Damage of porous building stone by sodium carbonate crystallization and the effect of crystallization modifiers

Encarnación Ruiz-Agudo [a],[*], Aurelia Ibañez-Velasco [a], Cristina Ruiz-Agudo [b],
Sarah Bonilla-Correa [a], Kerstin Elert [a], Carlos Rodríguez-Navarro [a]

[a] *Department of Mineralogy and Petrology, University of Granada, Spain*
[b] *Department of Chemistry/Zukunftskolleg, University of Konstanz, Germany*

ARTICLE INFO

ABSTRACT

Salt crystallization is an aggressive weathering mechanism affecting porous building materials. The extensive use of Portland cement, a source of alkalis, in modern buildings and restoration interventions makes sodium carbonate salts important weathering agents. Herein, we study salt damage to a porous stone commonly used in the Andalusian built heritage (Santa Pudia limestone) due to stress generation associated with the precipitation of natron ($Na_2CO_3 \cdot 10\ H_2O$). We performed cyclic crystallization tests combined with thermodynamic and poro-mechanical calculations to determine salt crystallization pressure and effective tensile stress suffered by the material. The outcome reveals that in-pore natron crystallization during cooling/evaporation generates stresses exceeding the tensile strength of the wet substrate, leading to extensive damage by fracturing and material loss. Damage is reduced using aminotris(methylenephosphonic) acid (ATMP), a common phosphonate-based crystallization modifier that induces non-damaging efflorescence growth as opposed to damaging subflorescence growth, which takes place in its absence.

1. Introduction

Crystallization of soluble salts is one of the most aggressive weathering mechanisms affecting the built heritage ([1–16]) as well as modern (cement-based) construction ([17–19]). Building materials intrinsically contain minimal amounts of soluble salts, but when water penetrates their porous network, it frequently carries dissolved saline species that can precipitate and induce salt damage. Additionally, damaging salts may originate from the chemical alteration of (i) the constituents of the building material itself or (ii) materials in the direct vicinity (e.g., cements) (Sebastián and Rodríguez-Navarro, 1994). Among the different mechanisms proposed to explain the damage caused by soluble salts, crystallization pressure is considered the most relevant ([20–22,4, 23–25,13,26]). The pressure exerted by a salt crystal when growing in a confined space (a pore) can easily overcome the tensile strength of most building and ornamental materials (including natural stone, mortars, concrete, and bricks), leading to their disintegration and crumbling [16]. Steiger, Scherer, and Coussy [21,23,24,26] separately derived equations for the calculation of the crystallization pressure considering both the degree of supersaturation and the effect of the curvature of the crystal-solution interface. These factors are related to the solvent supply and evaporation rate and/or undercooling (in salt systems with *T*-dependent solubility), which in turn are determined by the physical properties of the solution (surface tension and vapor pressure), environmental conditions, and characteristics of the pore system of the building material [4,7]. The combination of these factors determines whether the crystallization of salts occurs as subflorescence or as efflorescence, the latter being more striking but generally much less damaging than the former.

Despite extensive research on salt damage, some aspects related to the dynamics and mechanisms by which this weathering process occurs still need to be fully understood. For example, it has not yet been conclusively explained why some salts are more harmful than others. Thus, under the same conditions, salts such as sodium and magnesium sulfates and sodium carbonates are highly damaging, while others, such as sodium chloride, are not [3,4,10,13]. Interestingly, the most damaging salt systems exhibit several hydrated phases [1,7,10]. However, given their high solubilities and corresponding low interfacial tension values, these systems would be expected to crystallize at low supersaturation and generate low crystallization pressures [27]. While

significant progress has been made in the understanding of the damage mechanisms caused by sodium and magnesium sulfates [4,7,10], very few works have addressed the crystallization mechanisms of alkali carbonates and the deterioration processes induced by these salts.

The Na$_2$CO$_3$-H$_2$O system presents two stable mineral phases at standard conditions (natron, Na$_2$CO$_3$•10 H$_2$O, and thermonatrite, Na$_2$CO$_3$•H$_2$O) and a metastable heptahydrate phase (Na$_2$CO$_3$•7 H$_2$O). There is an additional anhydrous phase, natrite (Na$_2$CO$_3$), which does not precipitate in solution under ambient pressure/temperature conditions and, in air, rapidly hydrates to form thermonatrite. Consequently, this phase is very rare in natural environments. Other related phases, in this case in the NaHCO$_3$-H$_2$O system, are trona (Na$_3$(CO$_3$)(HCO$_3$)•2 (H$_2$O)) and nahcolite (NaHCO$_3$). The Na$_2$CO$_3$-H$_2$O system can be considered an analogue of the Na$_2$SO$_4$-H$_2$O system, as both have three distinct phases with varying degrees of hydration (anhydrous/monohydrated, heptahydrated, and decahydrated) [28]. Yet, it is important to study the Na$_2$CO$_3$-H$_2$O system to determine whether the conclusions reached regarding the alteration mechanisms induced by sodium sulfate crystallization [10,29] are general and valid for other hydrated systems. In addition, sodium carbonate salts have a high damage potential. They are typically ranked as the second most (and under particular conditions, even the most) deleterious salts for porous building materials after sodium sulfates [3,30]. It should also be considered that salt damage caused by sodium carbonate crystallization in historic buildings will likely increase significantly in the coming years due to the extensive use of Portland cement in conservation and restoration interventions in the recent past, as well as in the vast majority of modern constructions [17, 31].

Portland cement (PC) clinker contains significant amounts of alkali oxides (Na$_2$O and K$_2$O) mainly from the clay components present in the raw mix. The reaction between Na$^+$ and CO$_3^{2-}$ ions in the pore solution results in the formation of sodium carbonates, which can induce salt damage in PC-based materials and the surrounding building materials. Considering a typical value of 1 wt% Na$_2$O in cement [31,32], up to 17 kg of sodium carbonate per ton of cement would be formed upon carbonation. The crystallization of these salts within the porous network of a stone in direct contact with such an incompatible PC-based material would, therefore, be one of the main agents of deterioration. Indeed, Charola and Lewin (1979) [31] pointed to the alkaline leachates of PC as the main cause of salt damage by sodium carbonate affecting old buildings. This was demonstrated, for example, in the case of marble alteration in the Church of Santa Maria dei Miracoli in Venice, where the crystallization of sodium carbonates due to alkali leaching from the PC applied in a previous intervention was detected [33]. Madruga et al. (1994) [34] also identified damaging trona (Na$_3$H(CO$_3$)$_2$·2(H$_2$O)) in Villamayor sandstone (used in the built heritage of Salamanca, Spain) in direct contact with the aqueous leachate of PC. Overall, damage caused by sodium (bi)carbonate salt phases (natron, thermonatrite-natrite, trona, and nahcolite) in buildings where cement was used as a conservation/repair material [35–37] or as a primary binder in modern construction [17,38–40] has been widely reported. Furthermore, it is expected that many concrete buildings that are already considered an essential part of our built heritage, such as the buildings of Le Corbusier, Frank Lloyd Wright, or the W. Gropius (Bauhaus) school, are likely to be affected by alkali carbonate crystallization problems. This issue will worsen in the future as PC buildings age, a process that involves carbonation [41] and typically results in the formation of calcium carbonate [42] as well as sodium carbonate salts, the latter resulting in significant damage [17]. Even alkali-silica reactions in concrete can result in the leaching of highly alkaline solutions that, upon carbonation, generate deleterious sodium carbonates [43]. Apart from PC-based materials, alkali-activated cements and geopolymers can also generate sodium carbonate efflorescence/subflorescence upon carbonation, provoking physical salt damage [44–46] and their highly alkaline leachates could be a source of damaging alkali carbonate salts for the surrounding building materials.

It is thus necessary to carry out studies that provide information (i) on the crystallization mechanisms in the Na$_2$CO$_3$-H$_2$O system and (ii) on the deterioration processes induced by these salts before the design and application of specific conservation treatments for salt-laden building materials. The precipitation of hydrated salts may occur through different mechanisms [47]: (i) evaporation of the solvent; (ii) changes in temperature, as the solubility of some salts rapidly decreases with T, which is particularly important for sodium carbonate (as well as sodium sulfate) and (iii) in the case of hydrated salts, the dissolution of a (more soluble) lower hydrate and the precipitation of the (less soluble) higher hydrate [10,25]. The resulting damage, therefore, depends on the crystallization pathway. All these mechanisms may occur in the Na$_2$CO$_3$–H$_2$O system. In this work, we explored the reduction in temperature (bulk solution crystallization experiments) and the combination of a temperature decrease and evaporation of the solvent (artificial ageing tests by salt crystallization) as the mechanisms inducing sodium carbonate precipitation (Fig. 1). These scenarios are relevant for damage generation in porous building materials subjected to diurnal/seasonal T changes.

The lack of knowledge on the origins of salt crystallization damage has limited the development of conservation treatments that attack the root of the problem, acting on the causes and not only on the effects of this alteration phenomenon ([8,48]). In the last 20 years, the use of additives that modify crystallization processes (crystallization inhibitors or promoters) to prevent or reduce salt damage has been proposed by the authors [48–51,8–10,12]. Depending on their concentration and nature, additives ranging from ions or molecules to more complex macromolecules such as polymers can inhibit and/or promote crystal nucleation and growth [12]. Although it might seem counterintuitive initially, salt crystallization damage can be reduced by applying crystallization inhibitors and promoters. Additives that act as inhibitors increase the induction time, i.e., the period between the establishment of supersaturation and the formation of a new phase at a higher critical supersaturation [52]. Long induction times allow the transport of the salt solution to the surface of the porous substrate, where crystallization occurs as efflorescence, which is less harmful to the material than subflorescence [49]. Conversely, when additives act as crystallization promoters, crystallization occurs inside the pores at low supersaturation, generating low crystallization pressure and avoiding or minimizing damage to the substrate [10].

In this study, we aim to gain an in-depth understanding of the damaging mechanisms of sodium carbonate crystallization and the effect of a range of organic and inorganic additives (phosphonates and derivatives of (poly)carboxylic acids, as well as sodium tetraborate -borax-, commonly used as crystallization modifiers in industrial applications). Our final objective is to select the most suitable additive as a crystallization inhibitor/promoter to minimize the damage sodium carbonate induces in porous building materials. We have selected Santa Pudia limestone, a porous building stone widely used in Andalusia's architectural heritage, as a model substrate for this task. A combination of crystallization experiments in unconfined media and artificial ageing tests by salt crystallization, with thermodynamic and poromechanical analyses, was used here to investigate salt damage due to sodium carbonate (natron, Na$_2$CO$_3$·10 H$_2$O) formation and how this process was affected by crystallization modifiers.

2. Methodology

2.1. Materials

Na$_2$CO$_3$ solutions for unconfined crystallization tests (12% w/w, 1.28 mol kg^{-1} H$_2$O) and artificial ageing tests by salt crystallization (6% −0.60 mol kg^{-1} H$_2$O- and 12% w/w, see below) were prepared from anhydrous solid (Sigma Aldrich; purity > 99.7) and deionized MilliQ water (MilliQ filtration system, Millipore Corporation, pH 5.96, resistivity >18.2 MΩ cm) to which different amounts of crystallization
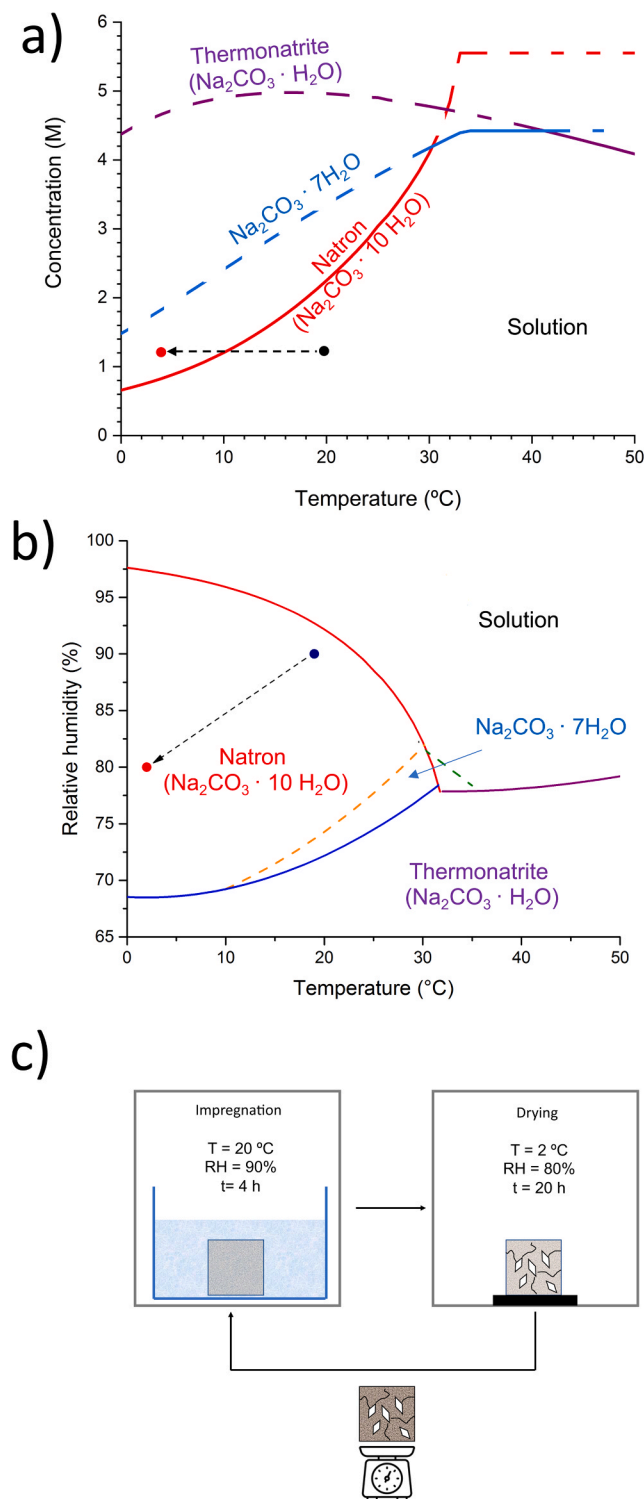
Fig. 1. Phase diagrams for the system Na_2CO_3-H_2O built using data from [47]: a) solubility vs. temperature and b) relative humidity vs. temperature. Pathways followed in bulk (unconfined) crystallization experiments and artificial ageing tests by salt crystallization are marked in a) and b), respectively. The black dot in a) denotes the conditions at the beginning of the bulk experiments, and the red dot marks the conditions upon precipitation. The black dot in b) keeps the conditions during the immersion step, while the red dot indicates the conditions during the drying of the stone (not immersed). For further details regarding the experiments, see the main text. c) Scheme of the artificial ageing tests by salt crystallization.

modifiers were added to give a final concentration of 0.1, 1, 10 and 100 mM. The additives chosen for the crystallization tests were: sodium citrate tribasic dihydrate (CA), L-aspartic acid sodium salt monohydrate (ASA), polyacrylic acid 2100 MW (PA), etidronic acid (HEDP), aminotris(methylenephosphonic) acid (ATMP), diethylene-triaminepentakis-(methylphosphonic) acid (DTPMP) and sodium tetraborate decahydrate (borax, $Na_2B_4O_7 \cdot 10$ H_2O). These compounds are commonly used as crystallization modifiers in industrial applications [12,51]. Artificial ageing tests by salt crystallization were performed on porous limestone, a calcarenite from Santa Pudia quarry, Granada (Spain), widely used in historical buildings in Granada. Geologically, it is a white to yellow calcarenite from the Tortonian deposits of the Guadalquivir Basin (Post-Orogenic Neogene Basins of the Betic Chains), composed primarily of a micritic calcite matrix and ca. 90% bioclasts. Other components include quartz, muscovite, and/or fragments of schist or gneiss. This calcarenite has an open porosity that ranges between 25–36% (25.2% in the case of the variety used in this study, determined using mercury intrusion porosimetry, MIP), an apparent density of 1730 kg m^{-3} and skeletal density of 2600 kg m^{-3}[53], a compressive strength (dry) ranging from 11–20 MPa and flexural strength (dry) of 2.8–5.1 MPa [54]. The calcarenite pore size distribution shows abundant macropores with a maximum at ca. 30 μm and a secondary maximum at ca. 0.1 μm [54]. Stones such as the studied calcarenite with a high proportion of pores with size < 1 μm connected to larger pores are very susceptible to salt weathering [55,56]. The submicrometer pores result in a larger surface area for evaporation and slower solution transport, thus increasing the chances that high supersaturation ratios are reached below the stone surface, resulting in detrimental sub-florescence growth. The hydric properties of the calcarenite (Ab, free water absorption: 15.8%); Af, forced water absorption: 19.8%; Ax, degree of pore interconnection: 20.1%; Di, drying index: 345; S, saturation coefficient: 71.3%; CC, capillarity coefficient; 496 g/m^2 s$^{0.5}$) show that, indeed, it rapidly absorbs water, but dries slowly, which negatively affect salt weathering susceptibility [53].

2.2. Crystallization tests in unconfined media

To identify which of the crystallization modifiers acts as inhibitors or promoters by increasing or lowering the supersaturation at which sodium carbonate crystallizes, bulk (unconfined) precipitation experiments were performed. A closed-jacketed glass reactor connected to a water bath for *T* control was filled with 100 mL of a 12% w/w sodium carbonate solution and stirred magnetically. The system *T* was lowered from 20 to 2 °C (Fig. 1a). 12% w/w sodium carbonate solution concentration was selected for these experiments as the optimal concentration for a stable solution at room temperature, which crystallizes upon cooling and before freezing. During the slow cooling of the solution, temperature, conductivity, and pH were monitored using Metrohm probes. At least three replicates of each experiment were performed to ensure reproducibility of the results. Since the crystallization of sodium carbonate is an exothermic process, an increase in the temperature of the solution marks the crystallization onset (as in [57] for sodium sulphate) (Fig. 2a, red arrow). Once precipitation was detected, crystals were separated from the solution by filtration and immediately analyzed by powder X-ray diffraction (XRD) to determine their mineralogy, using a Panalytical X'Pert PRO diffractometer (Cu Kα radiation, λ = 1,5405 Å, voltage 45 kV, current 40 mA, and scanning angle (°2θ) 3–70°, steps of 0001°2θ and goniometer speed of 0,01°2θ·s^{-1}).

2.3. Artificial ageing tests by salt crystallization

We measured the weight change of 3x3x3 cm^3 stone specimens of Santa Pudia limestone as a function of the number of cycles of complete immersion in 6% and 12% (w/w) sodium carbonate undersaturated solutions. This size was selected to ensure close-to-saturation conditions and complete drying during the artificial ageing tests by salt
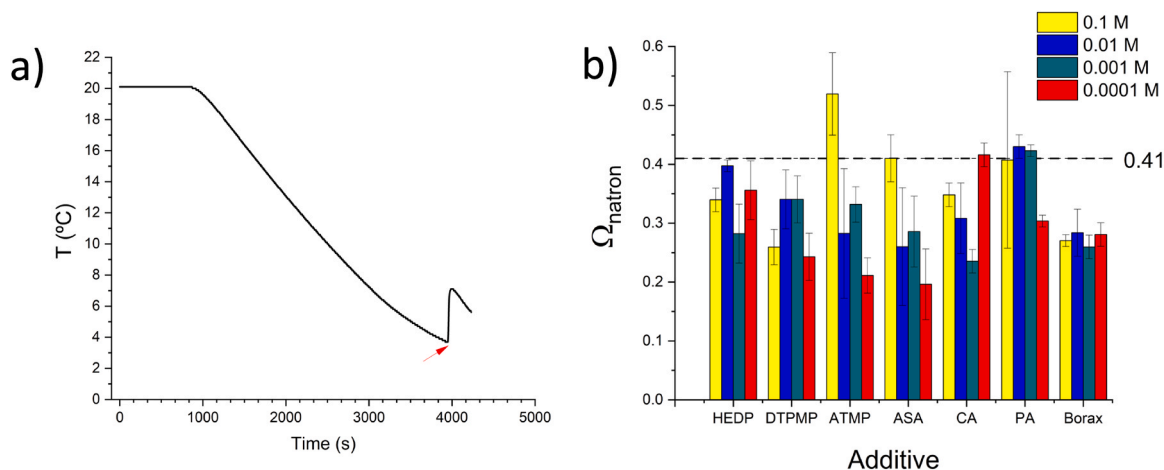
Fig. 2. a) Typical solution T vs. time evolution during the slow cooling of a 12% w/w Na_2CO_3 solution at a 0.6 °C/min rate. The onset of crystallization is marked by the sudden increase in T (red arrow) in bulk (unconfined) crystallization experiments. b) Threshold supersaturation (Ω) reached by 12% w/w Na_2CO_3 solutions during cooling at a 0.6 °C/min rate in the absence and presence of additives (dosed at the concentrations -in mmol/L- indicated in the top of the bar graphic).

crystallization so that these tests could be performed daily. Next to the 12% w/w concentration, a 6% concentration was used to make sure the very high salt concentration would not mask the effect of the modifier. Tests were performed in a climatic chamber model KMF 115 (BINDER GmbH, Tuttlingen, Germany), set at 20 °C and 90% RH during immersion for 4 h and at 2 °C and 80% RH during drying (not immersed) for 20 h (Fig. 1c). A maximum of 11 cycles were performed, and samples were weighted after the drying step. Considering the Na_2CO_3-H2O phase diagram (Fig. 1b), these conditions were chosen to enable the precipitation of $Na_2CO_3 \cdot 10\ H_2O$ and avoid its transformation into phases with a lower water content. Three stone specimens per condition were submitted to these crystallization tests. During the first cycle, the weight of the control sample (i.e., specimens submitted to crystallization tests in solutions without any additive) was continuously monitored to evaluate the change in solution concentration due to evaporation. Additionally, a core was drilled in the center of the stone specimens, and a thermocouple probe was introduced to monitor the temperature evolution inside the stone during the cooling/evaporation stage of the cycle. After the experiments, cross-sections of altered stone samples (i.e., cut normal to the sample evaporation surface using a diamond saw with ethyl alcohol as cooling fluid to avoid dissolution of the salts) were prepared to study morphology and texture using environmental scanning electron microscopy (ESEM, backscattered electron imaging mode) coupled with energy dispersive X-ray spectroscopy (EDX) to obtain element distribution maps. We carried out an image analysis of Na element maps for pore-filling estimation on three locations of each sample (samples weathered in additive-free and ATMP-bearing solutions). Segmentation was conducted using the threshold tool included in Adobe Photoshop, and the area associated with the salt was measured using this software, as indicated in [58].

Based on the results of the unconfined crystallization experiments and the weight change and visual observations of stone specimens submitted to artificial ageing tests by salt crystallization, it was decided to characterize unaltered limestone samples further. Samples weathered in the 6% w/w solution, with and without ATMP added, using MIP using Micromeritics Autopore III 9410 equipment with a maximum injection pressure of 414 MPa. For MIP measurements, we split the samples manually and collected cross-sectional specimens (i.e., including the core and the surface). One MIP measurement per type of sample was performed which was considered to be representative of the stone specimen since (i) the sample volume analyzed was close to 10% of the whole specimen submitted to the artificial ageing test and (ii) the calcarenite used is relatively homogenous (within a given variety) at the scale of stone specimens used here. This technique allows the analysis of

the stones´ pore system and its modification upon salt crystallization. In the case of MIP on altered limestone subjected to artificial aging, samples were measured before and after desalination. The surface roughness of these samples before and after weathering was analyzed using a Leica VDM2000 videomicroscope, and the data and images were processed using the Leica Application Suite v.3.8.0 and Leica Maps Start v.6 (Leica Microsystems©) software.

3. Results and discussion

3.1. Crystallization tests in unconfined media

Sodium carbonate decahydrate (natron) was the phase that precipitated in all bulk (unconfined) crystallization tests, identified by X-ray diffraction (Fig. S1). The threshold supersaturation (Ω, the supersaturation at which crystallization takes place) can be calculated as:

$$\Omega = \log\left(\frac{IAP}{k_{sp}}\right) \tag{1}$$

where IAP is the ion activity product, and k_{sp} is the solubility product of the relevant phase. This parameter allows evaluation of the effectiveness of the additives as inhibitors or promoters by comparison with the threshold supersaturation reached in the additive-free solution. In unconfined experiments, supersaturation is achieved by rapid cooling of the solution. The solubility product of natron and the heptahydrate (as the relevant phases under the conditions of our experiments) were calculated here using the expression:

$$\ln k_{sp} = A + \frac{B}{T} \tag{2}$$

where A and B are fitting parameters. We used the values in [59] (natron: A=28.3 and B= −9000 K; heptahydrate: A=19.9 and B= −6230 K). The IAP was calculated for a Na_2CO_3 solution with a concentration of 1.28 mol kg^{-1} H_2O (12% w/w) at the temperature of the crystallization onset, using the geochemical code PHREEQC [60] and the Pitzer database, suitable for non-ideal solution calculations at high ionic strengths.

In the control runs (i.e., those performed in the absence of additives), crystallization occurred at 4.40 ± 0.79 °C, corresponding to a supersaturation of the system with respect to natron at the time of crystallization (threshold supersaturation) of 0.41. On the contrary, the solution is undersaturated with respect to the heptahydrate at the moment of crystallization in all the experiments performed. This supports our hypothesis that direct (i.e., without any precursor phase) precipitation of

natron is taking place. Most of the additives studied acted as promoters of the crystallization of this phase when added to the salt solution at pH 11.4, which is the equilibrium pH of a 12% w/w sodium carbonate solution. The threshold supersaturation reached for the additive concentrations used was systematically lower than that of the control solution (Fig. 2b), except for ATMP, which acted as an inhibitor at the highest concentration tested here. Interestingly, in the case of ATMP and ASA, the threshold supersaturation reached tended to increase with additive concentration. At the same time, for borax, PA, CA, HEDP, and DTPMP, no clear trend was observed.

The observed promoting behavior may be due to the heterogeneous nucleation of sodium carbonate on the substrate (glass crystallizer), to which the additive molecules can adsorb. The glass-water interface is characterized by acidic Si-O$^-$ groups due to deprotonated OH-groups on the silica glass surface [61]. The point of zero charge (PZC) of silica is pH 1.8–3 [62]. Hydroxyl groups, therefore, deprotonate at pH>PZC, and an increase in glass surface negativity is expected with increasing pH. Thus, the adsorption of organic compounds on the support glass would occur through the interaction between non-deprotonated functional groups in the additives and Si-O$^-$. In the case of ATMP, DTPMP, and HEDP, this process likely consists of the formation of hydrogen bonds between the Si-O$^-$ groups of the substrate and protonated acidic groups in the additives, aided by the presence of a hydroxyl group in the case of HEDP. It is well-known that phosphonates strongly tend to adsorb on various surfaces, including silicates (silica and clay minerals), calcite, barite, cassiterite, aluminum, and iron oxides [63,64]. In the case of CA and ASA, this process probably involves the formation of hydrogen bonds between the Si-O$^-$ groups of the substrate and hydroxyl and amino groups in the additives. Limited interaction is expected in the case of PA since it is fully deprotonated at the experiments' pH; indeed, this additive induces the least changes in the crystallization of sodium carbonate. Finally, the interaction with borax likely occurs through the hydroxyl groups of the tetra-coordinated borate ions B(OH)$_4^-$, the dominant species at the pH of our experiments. Adsorption of these additives can facilitate the heterogeneous nucleation of natron on the glass wall by surface energy reduction. The layers of adsorbed organic molecules are expected to act as a template fostering the heterogeneous nucleation of natron at relatively low supersaturation, as it has been described for other minerals in natural (biomineral) and artificial environments [65]. This phenomenon could explain the observed systematic precipitation of natron on the surface of glass crystallizers in the presence of additives at lower supersaturation than in control runs. As the concentration of the additive increases, an excess of the additive will be in the solution and may exert an inhibitory action. This might explain the positive relation between threshold supersaturation and additive concentration [66]. These results indicate that in the case of SiO$_2$-rich ornamental stones (for example, sandstones) or cement-based materials subjected to alteration by crystallization of natron, additives can induce precipitation at low supersaturation, reducing the crystallization pressure and damage caused by this salt. Conversely, the additives acting as crystallization inhibitors (e.g., ATMP dosed at the highest concentration tested here) could favor the formation of harmless efflorescence. Considering the experimental results from this first screening test, we selected ATMP (100 mM) and ASA (0.1 mM), which showed the best performance as crystallization inhibitors and promoters, respectively, to test their effectivity at reducing damage to porous limestone during cyclic crystallization of sodium carbonate, mimicking salt weathering.

3.2. Experimental analysis of sodium carbonate damage to a porous substrate and the effect of additives

Fig. 3 shows the temperature evolution within the climatic chamber and the stone specimen and the weight loss of the stone specimen during the cooling (and drying) step of the first cycle for experiments performed using both 6% and 12% w/w solutions. Tables S1 and S2 display the evolution of the pore solution concentration (determined from weight
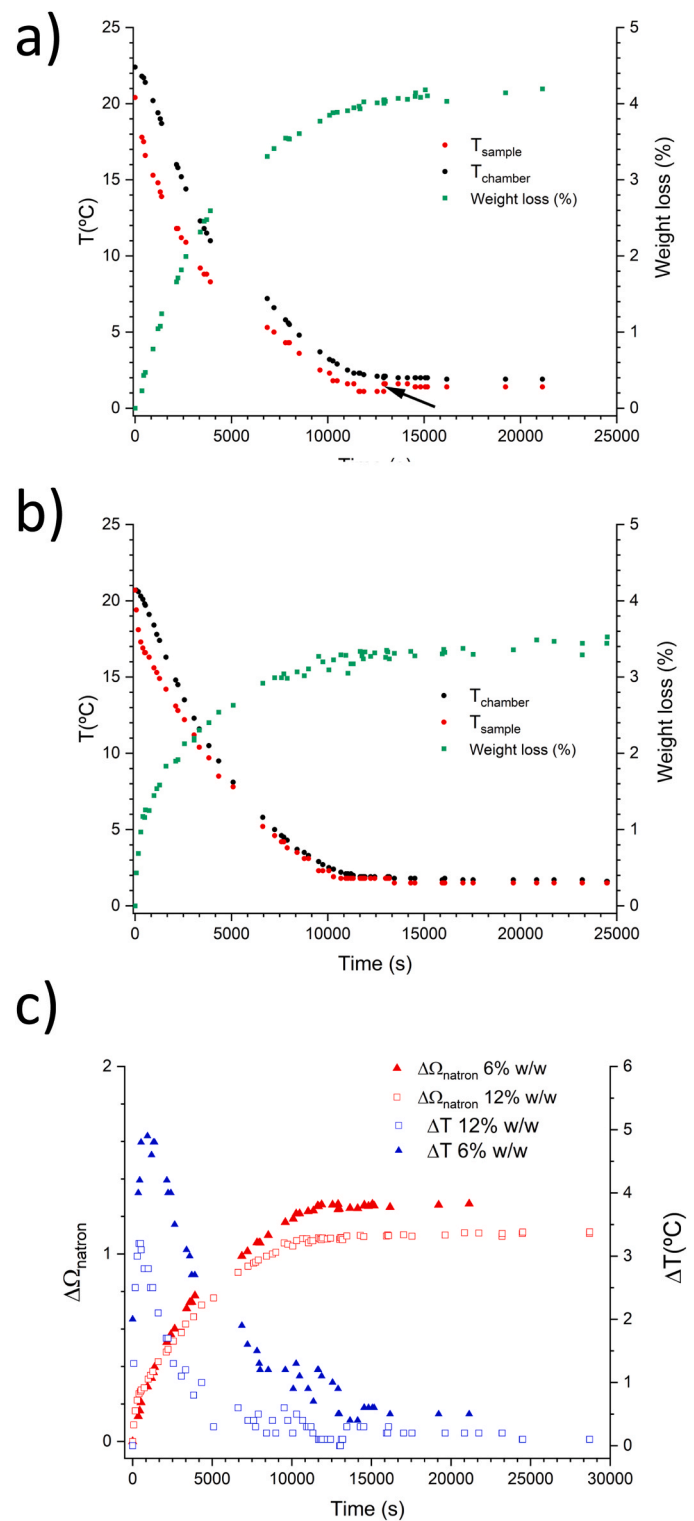

Fig. 3. Time evolution of temperature within the chamber and in the stone interior and the weight loss of the stone specimen during the first cycle's cooling (and drying) step for artificial ageing tests performed using a) 6 and b) 12% w/w solutions. The arrow in (a) marks the onset of natron crystallization (marked by a sudden T increase). c) Time evolution of the difference between the temperature in the chamber and in the interior of the stone specimens and of the difference in the supersaturation of the solution (Ω_{natron}) of the pore solution with respect to the initial Ω_{natron} of the solutions for experiments performed using both 6% and 12% w/w solutions.

continuous monitoring), activities of the different ions, *IAP,* and supersaturation with respect to natron and heptahydrate (calculated using PHREEQC) as a function of sample temperature. Interestingly, the temperature within the stone is several degrees lower than that of the chamber during the first part of the cooling step. However, both temperatures tend to converge once solvent evaporation ceases (Fig. 3c). This can be understood if we consider that water evaporation also takes place during the cooling of the stone specimens. Evaporation is an endothermic process that cools the wet stone substrate below the chamber temperature. In the experiments performed using a solution with an initial concentration of 6% w/w, a temperature as low as 1.1 °C was measured in the interior of the stone sample, even though the chamber temperature was 1.9 °C. At that point, a sudden increase in temperature within the stone up to 1.6 °C was observed, which was associated with the onset of $Na_2CO_3 \cdot 10\,H_2O$ crystallization (black arrow in Fig. 3a). The pore solution's concentration at the crystallization point was calculated to be 1.07 M (10.3% w/w) (Table S1). In the experiments performed using a solution with an initial concentration of 12% w/w, the temperature within the stone also decreases below that of the chamber during the first part of the cooling step, although this effect is less pronounced (Fig. 3b). Note that several studies have shown that increasing the salt concentration in solution reduces the evaporation rate from porous media ([67] and references therein). Thus, in the 6% w/w solution, evaporation (and associated evaporative cooling) occurs at a faster rate, and despite the lower absolute values of supersaturation during the experiments compared to the 12% w/w solution, there is a faster change in supersaturation during the experiment (see the evolution of $\Delta\Omega_{natron}$ in Fig. 3c for both solutions). Since the nucleation rate is directly related to the cooling rate (Mullin et al., 1970), faster cooling rates favor nucleation over growth (i.e., more crystals with smaller sizes would form under these conditions). In contrast, the 12% w/w solution has a slower evaporation (and cooling) rate compared to the 6% w/w solution, which would favor crystal growth over nucleation (so fewer crystals with bigger sizes would form). This could explain why the thermal event associated with sodium carbonate nucleation is not detected in the case of the solution with the higher (12% w/w) initial concentration (Fig. 3b).

Fig. 4 shows the results of the weight change of Santa Pudia limestone specimens during cycling *RH-T* tests in the absence and presence of ATMP and ASA. It can be observed that all samples initially gain approximately the same weight. However, in the case of the control and aspartate-bearing samples, they begin to lose weight between the second and third cycles. On the contrary, the weight of the samples containing ATMP (only for the experiments performed using the 6% w/w solution, Fig. 4a) remains approximately constant from the second cycle onwards, showing a significant damage reduction due to this additive's presence. Weight measurements agree well with visual observations of the damage suffered by the stone specimens (Fig. 5a). Control and aspartate-bearing samples show evidence of severe weathering after 11 cycles, with significant loss of cement between grains, which can also be detected in the surface rugosity analysis (Fig. 5b). However, ATMP samples are only slightly altered showing very subtle superficial damage, and ageing tests were stopped after nine cycles since the weight of stone specimens was virtually constant since the third cycle. Backscattered electron images and elemental maps of cross-sections of the stone specimens show that in the presence of ATMP, salts are concentrated close to and on the surface of the stone specimens (Figs. 6c, 6d). In contrast, in control runs, salts appear evenly distributed throughout the sample (Fig. 7), and significant material cracking is associated with salts (Figs. 6a, 6b). The image analysis of Na elemental maps provided values of the area related to the salt ranging from 30.7 to 32.2% for the samples weathered in additive-free solutions. Note that these values are very similar to the overall porosity measured by MIP after salt removal (29.3%) of these samples, showing that at least in the center of the stone specimens where the SEM images were obtained, complete filling of the pore space was achieved. In the case of the samples weathered in ATMP-bearing solutions, significantly lower values were measured (7.3–18.2%), corresponding to percentages of pore filling ranging from (26 to 64%) in the center of the stone specimens. Although the different areas analyzed yield similar results within a given sample, it must be considered that the overall area studied by SEM-EDS is a small part of the whole specimen. Therefore, a degree of uncertainty may be present in this analysis.

In control (additive-free) samples, weathered in 6% w/w solutions, natron crystallization results in an increase in the overall porosity of the samples (from 25.2% of the unaltered samples to 29.3% of the weathered sample after salt removal) and a significant increase in the volume of pores with size > 1 µm after 11 aging cycles, which are absent in the unaltered samples (Fig. 8). This is consistent with the extensive cracking observed in SEM images. A new maximum can be observed in the pore size distribution plot of weathered samples, corresponding to pores between 10–100 µm. Natron fills mostly the new pores of size > 1 µm generated upon weathering. In the case of the weathered ATMP sample, a smaller increase (compared to the control sample) in porosity (28.2%) and volume of pores of size > 1 µm was observed after 11 aging cycles. The volume of the pores of size 0.3 µm slightly increases after the artificial ageing tests, and salts are located both within these pores (already
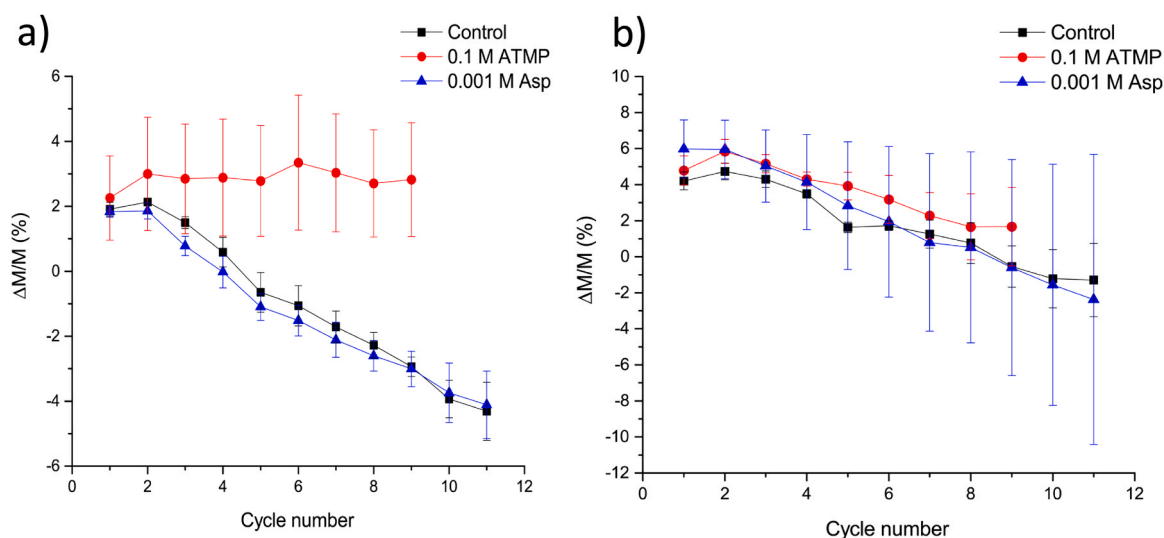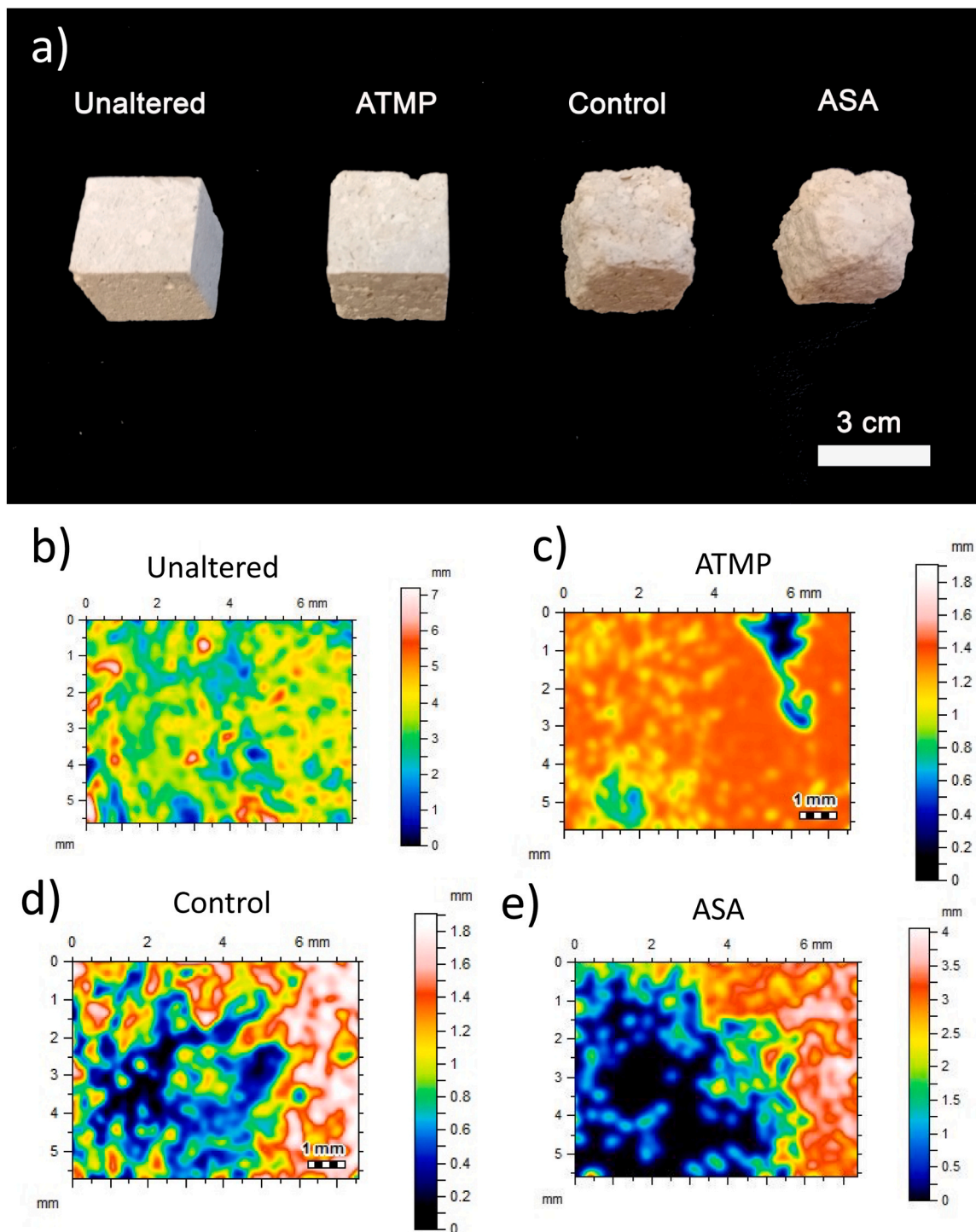

Fig. 4. Weight change of Santa Pudia limestone samples as a function of the number of salt crystallization cycles using (a) 6% (w/w) and (b) 12% (w/w) sodium carbonate solutions. The error bars correspond to one s.d. Three samples were used for each crystallization test.

Fig. 5. a) Santa Pudia limestone samples before (unaltered) and after (ATMP, control, ASA) salt crystallization cycles in 6% w/w sodium carbonate solutions. b) 3D surface maps of ATMP and control limestone specimens shown in a), the latter revealing a marked increase in surface roughness due to granular disintegration and material loss, which is nearly absent in the sample weathered in the presence of ATMP. ATMP limestone specimens were submitted to 9 cycles, and the remaining samples were submitted to 11 cycles (see text for further details).

present in the original material) and in the newly developed pores of size > 1 μm. Overall, our artificial ageing tests demonstrate that severe damage to porous materials can occur due to in-pore natron crystallization and the simultaneous generation of significant crystallization pressure and that, for moderate salt loads, such damage can significantly be reduced by the addition of a crystallization inhibitor such as ATMP.

3.3. Thermodynamic and poromechanical analysis of macroscopic tensile stress generation during sodium carbonate crystallization

We followed and combined the approaches described in [10,29,47], adapting them to our experimental design aimed at evaluating the damage related to direct natron crystallization upon cooling and drying. The crystallization pressure (p) exerted by a crystal growing in a pore can be calculated according to [68]:
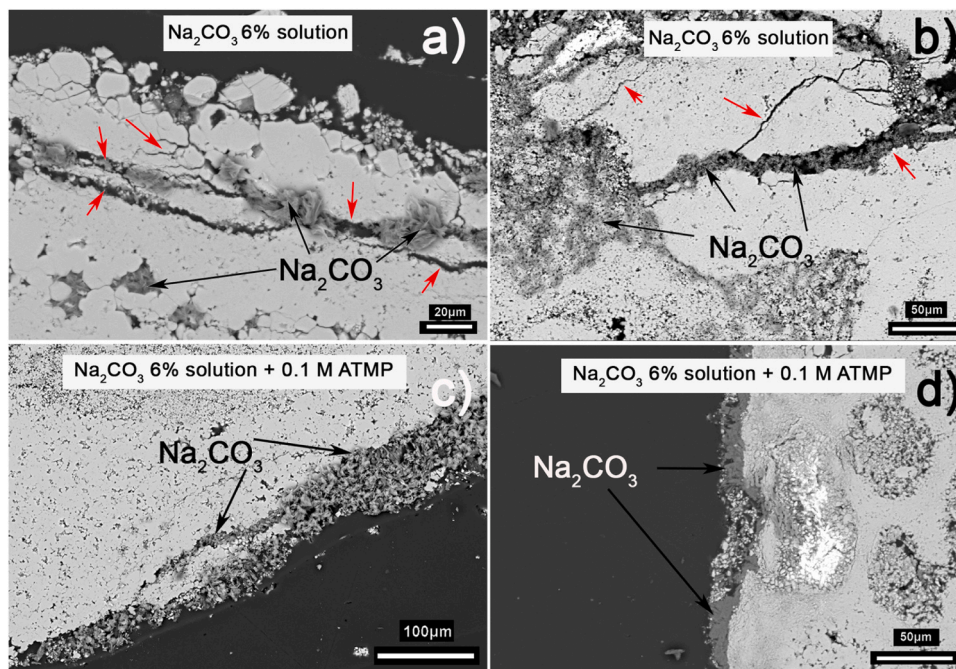
Fig. 6. Backscattered ESEM images of cross sections of limestone specimens after completion of artificial ageing tests by salt crystallization (6% solutions). a) and b) correspond to control runs (no additive in solution) (11 cycles) and c) and d) correspond to tests performed in the presence of 100 mM ATMP (9 cycles). Images show the upper part of the stone specimens. Note the preferential distribution of the salts in the outermost surface layer of the stone in the case of the experiments performed in the presence of 100 mM ATMP. Numerous cracks (marked with red arrows) filled with sodium carbonate crystals are observed in the case of the control runs.
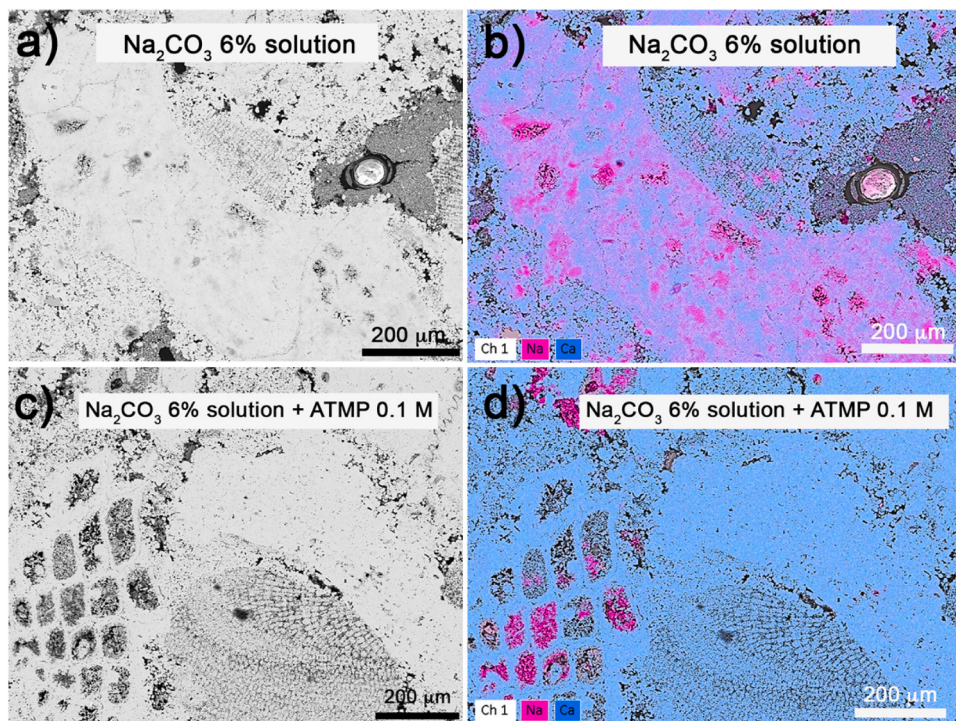
Fig. 7. Backscattered ESEM images (a, c) and elemental maps (b, d) of cross sections of limestone specimens after completion of artificial ageing tests by salt crystallization (6% solutions). a) and b) correspond to control runs (no additive in solution) (11 cycles) and c) and d) correspond to tests performed in the presence of 100 mM ATMP (9 cycles). Images correspond to the interior of the stone specimens. Sodium carbonate appears distributed homogeneously within the stone pore network of the control runs, while only a minimal amount of sodium carbonate in the interior of the material was observed in the case of the experiments performed in the presence of 100 mM ATMP.
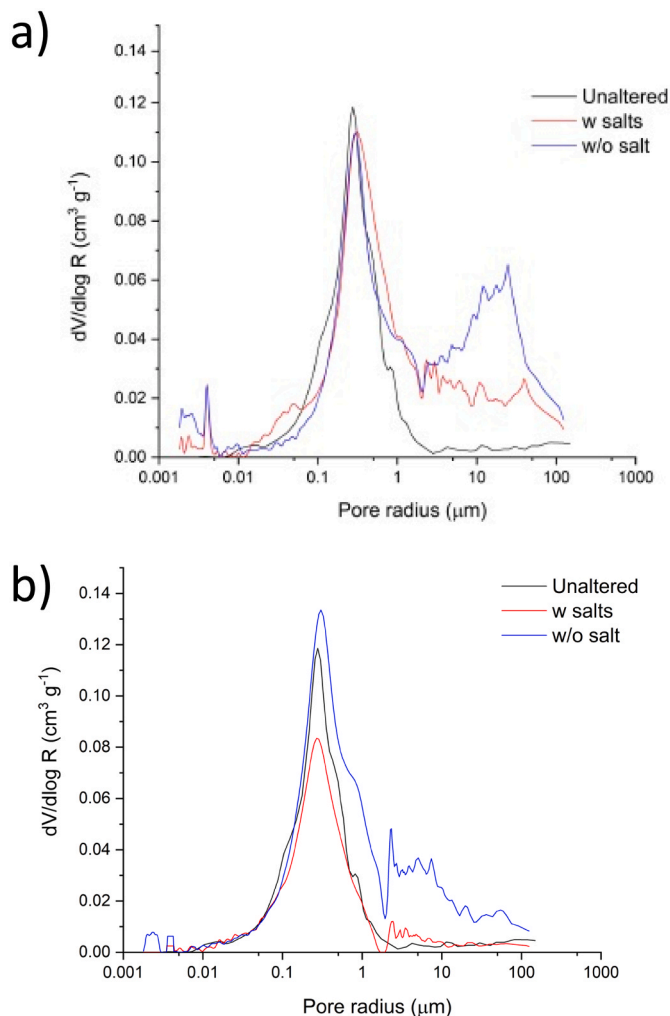
Fig. 8. Pore size distribution of stone specimens before (unaltered) and after artificial ageing tests by salt crystallization (with and without removal of salts by repeated washing in deionized water), obtained by Hg intrusion porosimetry (MIP). a) Control (11 cycles) and b) ATMP (9 cycles) samples artificially aged in 6%w/w Na_2CO_3 solution.

$$p = \frac{R \cdot T}{V_m} \cdot \ln \frac{IAP}{k_{sp}} - \gamma_{cl} \cdot \kappa_{cl} + \frac{\Delta V}{V_m} \cdot \gamma_{lv} \cdot \kappa_{lv} \qquad (3)$$

where R is the gas constant, $\Delta V = V_L - V_m$, $V_L = \Sigma V_i$ is the sum of the ionic molar volumes, V_m is the molar volume of the salt, k_{cl} and k_{lv} are the curvatures of the crystal-liquid and vapor-liquid interfaces, respectively, and γ_{cl} and γ_{lv} are the surface energies of the crystal-solution and vapor-solution interfaces, respectively. The first term indicates the thermodynamic control over the crystallization process through supersaturation of the system, which is the driving force for salt damage. The second and third terms are negligible in materials with pore size > 100 nm [27], as is the case of the porous limestone tested here.

The crystallization pressure calculated in this way is not directly equal to the stress generated during a crystallization event since it is unlikely that the latter is effectively transmitted to the entire stone volume [69]. Assuming that the salt is homogeneously distributed within the porous medium, averaging the stress over a representative element of it, the macroscopic tensile stress, $\sigma *$, can be estimated as follows:

$$\sigma^* = \sigma_r \cdot b \cdot S_c \qquad \text{Eq.4}$$

where b is the Biot's coefficient, S_c is the fraction of the porous volume

filled with salts (see Supplementary Information for details on its calculation) and $\sigma_r \approx p$ is the radial compressive stress. It is estimated that the critical stress of the material (i.e., when the material is expected to fail), σ_C^*, is given by:

$$\sigma_c^* = \frac{\sigma_T}{\sqrt{3 \cdot (1 - 2 \cdot \upsilon)}} \qquad (5)$$

where ν is the Poisson coefficient, and σ_T is the tensile strength. For limestone with a porosity of 25.2%, a Biot's coefficient of ca. 0.75 can be estimated (Cosenza et al., 2002). Considering that for this (dry) material $\sigma_T = 1.8$ MPa [10] and $\nu = 0.35$ [70], the critical stress at which the Santa Pudia limestone would fail is 1.9 MPa.

In our experiments performed using an initial 6% w/w solution, we discarded the initial formation of heptahydrate and its subsequent transformation into natron, as it has been shown, for example, in the case of sodium sulfate during cooling crystallization experiments [69], because the solution remained undersaturated with respect to heptahydrate in the temperature range of the weathering experiments (Table S2). During the first cycle, the fraction of pores filled with natron (S_c) is calculated to be 0.12. This fraction represents an increase in the weight of our stone specimens of 2.31%, which is in good agreement with the experimentally determined increase in weight for the first cycle of the control ($\Delta M/M = 1.91 \pm 0.21\%$), ATMP ($\Delta M/M = 2.25 \pm 1.29\%$) and aspartic ($\Delta M/M = 1.83 \pm 0.16\%$) experiments using 6% w/w solutions. Damage is expected to occur during the drying/cooling stage from the second aging cycle onwards, when a macroscopic tensile stress of 2.6 MPa is generated due to natron crystallization at 1.1 °C, overcoming the critical strength of the material (Fig. 9). These calculations are performed assuming that salts are homogeneously distributed and that limited transport of the solutes takes place during drying.

However, the solution flows towards the surface during drying, and ions are transported by advection towards the evaporation surface. Consequently, a concentration gradient develops, but diffusion tends to act towards leveling the solution concentration. Therefore, a competition between advection and diffusion is established, whose magnitude can be estimated by calculating the Péclet number defined by Pe ≡ $\overline{U}$L/ D, where L (m) is the length of interest (i.e., the size of the stone specimen), D (m²/s) is the ion diffusion coefficient and $\overline{U}$ is the average solution flow velocity given by $\overline{U}$ = J/A/ρₗ/ø, where J (kg/s) is the evaporation rate, A (m²) is the surface area of the evaporation front, ρₗ (kg/m³) is the solution density and ø is the pore fraction.

Note that when Pe >> 1, advection is the dominant ion transport mechanism, while diffusion is dominant when Pe << 1. In the case of sodium carbonate in solution, we consider a D value of 0.742×10^{-9} m²/s (at 25 °C, 0.5 M concentration) [71]. Values of $\overline{U}$ during drying were calculated from weight loss measurements. These values were used to calculate Pe. In our experiments, Pe values at the moment of crystallization are approx. 5, suggesting that ion transport could be controlled by advection when crystallization occurs in our experiments, resulting in the development of concentration gradients within the sample. However, our SEM observations seem to reflect a pretty homogenous distribution of the salt, at least in the control (additive-free), weathered sample. In the case of the ATMP-doped solution, in contrast, the salt seems to be concentrated in the outer layers of the sample. In any case, and due to the difficulties in unambiguously determining the exact concentration of the salt at the onset of crystallization (and the influence on it of concentration gradients), as well as the stone volume affected, our calculations establish a lower limit for the actual concentration at the onset of crystallization. This value could be even higher due to kinetic effects and, in any case, is indicative of the damaging character of sodium carbonate. Moreover, since these calculations agree well with the observed onset of damage in our experiments, we are confident that concentration gradients are not critical.

Our weight measurements do not reflect damage in the second cycle ($\Delta M/M = 2.12 \pm 0.08\%$) since the initial weight loss related to incipient

a)

b)
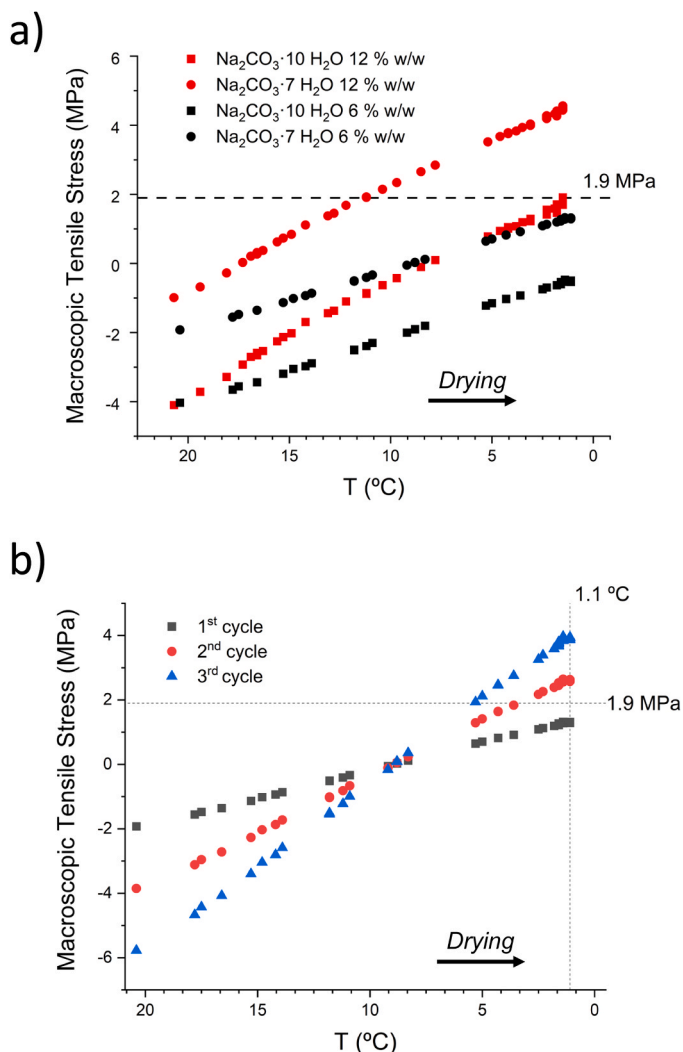
Fig. 9. (a) Macroscopic tensile stress developed during the first drying (cooling) step in stone weathering experiments as a function of the temperature within the stone specimen, calculated assuming heptahydrate ($Na_2CO_3 \cdot 7\ H_2O$) or natron ($Na_2CO_3 \cdot 10\ H_2O$) crystallization, and S_c (fraction of filled pores) of 0.12, for experiments performed using a 6% w/w solution and S_c of 0.25 for a 12% w/w solution. Note that negative tensile stresses are due to the undersaturated state of the saline solution; these values thus have non-physical meaning. (b) Macroscopic tensile stress developed during the drying (cooling) step of three consecutive aging cycles as a function of the temperature within the stone specimen, calculated assuming natron ($Na_2CO_3 \cdot 10\ H_2O$) crystallization, and S_c of 0.12, 0.25, and 0.37 for experiments performed using a 6% w/w solution. The horizontal dashed line in a) and b) marks the critical stress that must be reached to produce damage in the dry limestone (1.9 MPa). The vertical line in b) marks the temperature at which the crystallization onset occurs according to temperature measurements. See the main text and supplementary information for details on this calculation.

damage may be compensated by further uptake of salts. Indeed, during the second cycle, an increase in the weight of the stones up to 4.62% (S_c=0.25) should have occurred due to a higher fraction of salt filling the pores. Interestingly, during this cycle, the ATMP samples (which show limited damage compared to the control samples) increased their weight up to $\Delta M/M = 3.00 \pm 1.74\%$. In our experiments, the weight of the control samples does not start to decrease significantly before the third cycle. This shows that even though damage due to crack generation and incipient weight loss could begin in the second cycle, it would not manifest in the measured weight loss until the third cycle.

Interestingly, in the case of the initial 12% w/w solution, the pore

solution becomes supersaturated with respect to the heptahydrate for temperatures lower than 8.5 °C. However, temperature measurements could not detect the crystallization onset in weathering experiments. As a threshold value, we can assume that crystallization occurs at a temperature equal to or below that measured in the unconfined experiments for natron crystallization (4.4 °C). However, it is reasonable to assume that the heptahydrate could form in our system since (i) metastable phases have lower interfacial energies as compared to the equilibrium phase, and (ii) in the $Na_2SO_4-H_2O$ system, it has been experimentally shown by nuclear magnetic resonance (NMR) that heptahydrate is the phase that forms most readily when samples are cooled [72]. In any case, heptahydrate crystallization during the first cycle will not damage the stone since the maximum stress reached is below the critical strength of the substrate during the entire cooling step (Fig. 9a). Indeed, the calculated S_c value of 0.25 for the first cycle would represent an increase in weight of our stone specimens of 4.73%, which is in good agreement with the experimentally determined increase in weight for the first cycle of the control ($\Delta M/M = 4.20 \pm 0.49\%$), ATMP ($\Delta M/M = 4.78 \pm 0.80\%$) and aspartic ($\Delta M/M = 5.97 \pm 1.60\%$) experiments using 12% w/w solutions. The heptahydrate formed in the first cycle likely dissolves until equilibrium is reached during the immersion step of the second cycle. Providing that the heptahydrate is present, the solution concentration will be given by the solubility of the heptahydrate. Our calculations using PHREEQC show that the resulting solution -in equilibrium with the heptahydrate- will be supersaturated with respect to natron ($\Omega = 0.18$, with a concentration of sodium carbonate of 1.58 M) during the immersion step at 20 °C. Using Corren's equation (Eq. 1), the crystallization pressure of natron precipitation after heptahydrate dissolution is calculated to be 5.0 MPa, which corresponds to a macroscopic tensile stress of 1.2 MPa calculated as described above, assuming a filled pore fraction of 0.31 (see Supplementary Information). The associated tensile stress could be high enough to damage the stone during the immersion step since the resistance of a moisture-saturated material is up to 40% lower than that of the dry material, i.e., 1.1 MPa [10]. Cooling and evaporation during the drying step would result in natron growth (at equilibrium) and provoke no damage.

In the experiments performed in the presence of ATMP using a 6% w/w Na_2CO_3 solution, the pressure exerted by natron crystallization is expected to be higher since precipitation occurs at a lower temperature due to the inhibitory effect of the additive. However, the salt is not homogeneously distributed within the stone substrate but is mainly concentrated close to and on the surface of the stone specimen (Figs. 6 and 7) so that the stress is not transmitted to the entire stone volume, which reduces the damage to the material. Indeed, some damage is observed near the surface in the form of cracks and loss of cohesion, for example, in Fig. 6c. This positive effect is not observed in the case of the 12% w/w solution, possibly due to the higher salt load of the material, which affects a significant volume of the stone. Alternatively, a different damage mechanism associated with heptahydrate to natron transformation might be at play here. No differences in the salt distribution or damage pattern compared with the control were observed in the presence of aspartic acid, even though it acted as a crystallization promoter in unconfined crystallization experiments. The latter is likely since the porous stone has a larger surface area than the glass reactor, so the limited amount of adsorbed aspartate ions would not be able to sufficiently cover the stone pore walls to form an effective template and enable heterogeneous nucleation of natron at low supersaturation.

4. Conclusions

Our artificial ageing tests and thermodynamic calculations of crystallization pressure and associated stress suggest that direct crystallization of natron upon decreasing *T* generates stresses high enough to damage porous limestone, although a relatively high salt load is required. Our calculations indicate that it is possible to cause damage in this system via the formation of the heptahydrate, followed by its

dissolution and subsequent natron precipitation. The direct thermodynamic approach used here provides information on the potential weathering activity of sodium carbonate, allowing the estimation of the stress generated due to its crystallization within porous materials and explaining the observed damage onset. Most additives tested as potential natron crystallization modifiers acted as crystallization promoters in bulk (unconfined) experiments, except for ATMP, which inhibits natron crystallization at high additive concentrations. For moderate salt loads and direct natron crystallization upon cooling and evaporation, this additive significantly diminishes the damage and the associated weight loss of the stone substrate, thus representing a promising strategy for reducing the deterioration of porous building materials related to the precipitation this hydrated sodium carbonate phase. Extremely large salt loads, such as the highest concentration tested here, might result in severe damage but are not expected to be common in real-case scenarios. Thus, additives will most likely be effective under real conditions. In a real case scenario, the additive could be applied as an aqueous solution by spraying or poulticing. Further tests should be performed to select the optimal application procedure in real case scenarios so that the maximum penetration of the additive could be achieved without leading to any damage to the substrate since wetting of a substrate having a high salt load may cause damage in case dissolution and reprecipitation at high supersaturation occurs. Future studies will be conducted to experimentally determine the sodium carbonate phase evolution during cooling and evaporation within porous materials.

CRediT authorship contribution statement

Ruiz-Agudo Cristina: Writing – review & editing, Methodology, Investigation. **Ibañez-Velasco Aurelia:** Methodology, Investigation. **Ruiz-Agudo Encarnacion:** Writing – review & editing, Writing – original draft, Supervision, Conceptualization. **Rodriguez-Navarro Carlos:** Writing – review & editing, Supervision, Funding acquisition. **Elert Kerstin:** Writing – review & editing, Methodology, Investigation. **Bonilla-Correa Sarah:** Methodology, Investigation.

Declaration of Competing Interest

The authors declare that they have no known competing financial interests or personal relationships that could have appeared to influence the work reported in this paper.

Data Availability

Data will be made available on request.

Acknowledgments

Appendix A. Supporting information

Supplementary data associated with this article can be found in the online version at doi:10.1016/j.conbuildmat.2023.134591.

References

[1] I.S. Evans, Salt crystallization and rock weathering: a review, 1970.
[2] B. Smith, B. Whalley, V. Fassina, Elusive Solution to Monumental Decay, N. Sci. 118 (1615) (1988) 49–53.
[3] A.S. Goudie, H.A. Viles, Salt Weathering Hazards, Wiley, 1997.
[4] C. Rodriguez-Navarro, E. Doehne, Salt weathering: Influence of evaporation rate, supersaturation and crystallization pattern, Earth Surf. Proc. Land 24 (3) (1999) 191–209.
[5] C. Rodriguez-Navarro, E. Doehne, Time-lapse video and ESEM: Integrated tools for understanding processes in situ, Am. Lab 31 (10) (1999) 28 (-+).
[6] E. Ruiz-Agudo, B. Lubelli, A. Sawdy, R.P.J. Hees, C. Price, C. Rodriguez-Navarro, An integrated methodology for salt damage assessment and remediation: The case of San Jerónimo Monastery (Granada, Spain), Environ. Earth Sci. 63 (2010) 1475–1486.
[7] E. Ruiz-Agudo, F. Mees, P. Jacobs, C. Rodriguez-Navarro, The role of saline solution properties on porous limestone salt weathering by magnesium and sodium sulfates, Environ. Geol. 52 (2) (2007) 305–317.
[8] E. Ruiz-Agudo, C.V. Putnis, L. Pel, C. Rodriguez-Navarro, Template-assisted crystallization of sulfates onto calcite: implications for the prevention of salt damage, Cryst. Growth Des. 13 (1) (2013) 40–51.
[9] E. Ruiz-Agudo, C.V. Putnis, C. Rodriguez-Navarro, Interaction between epsomite crystals and organic additives, Cryst. Growth Des. 8 (8) (2008) 2665–2673.
[10] M. Schiro, E. Ruiz-Agudo, C. Rodriguez-Navarro, Damage mechanisms of porous materials due to in-pore salt crystallization, Phys. Rev. Lett. 109 (26) (2012).
[11] A.E. Charola, Salts in the deterioration of porous materials: an overview, J. Am. Inst. Conserv 39 (3) (2000) 327–343.
[12] C. Rodriguez-Navarro, L.G. Benning, Control of crystal nucleation and growth by additives, Elements 9 (3) (2013) 203–209.
[13] R. Flatt, N. Aly Mohamed, F. Caruso, H. Derluyn, J. Desarnaud, B. Lubelli, R. M. Espinosa Marzal, L. Pel, C. Rodriguez-Navarro, G.W. Scherer, N. Shahidzadeh, M. Steiger, Predicting salt damage in practice: A theoretical insight into laboratory tests, RILEM Tech. Lett. 2 (0) (2017) 108–118.
[14] S. Godts, M. Steiger, S.A. Orr, A. Stahlbuhk, J. Desarnaud, H. De Clercq, V. Cnudde, T. De Kock, Modeling salt behavior with ECOS/RUNSALT: terminology, methodology, limitations, and solutions, Heritage 5 (4) (2022) 3648–3663.
[15] C.T. Oguchi, S. Yu, A review of theoretical salt weathering studies for stone heritage, Prog. Earth Planet Sc. 8 (1) (2021).
[16] E. Winkler, Stone in Architecture: Properties, Durability, Springer Berlin Heidelberg, 1997.
[17] H. Haynes, R. O'Neill, M. Neff, P.K. Mehta, Salt weathering of concrete by sodium carbonate and sodium chloride, Acids Mater. J. 107 (3) (2010) 258–266.
[18] M.R. Sakr, M.T. Bassuoni, Performance of concrete under accelerated physical salt attack and carbonation, Cem. Concr. Res 141 (2021).
[19] M.R. Sakr, M.T. Bassuoni, R.D. Hooton, T. Drimalas, H. Haynes, K.J. Folliard, Physical salt attack on concrete: mechanisms, influential factors, and protection, Acids Mater. J. 117 (6) (2020) 253–268.
[20] G.W. Scherer, Crystallization in pores, Cem. Concr. Res 29 (1999) 1347–1358.
[21] G.W. Scherer, Stress from crystallization of salt, Cem. Concr. Res 34 (9) (2004) 1613–1624.
[22] C. Rodriguez-Navarro, E. Doehne, E. Sebastian, How does sodium sulfate crystallize? Implications for the decay and testing of building materials, Cem. Concr. Res 30 (10) (2000) 1527–1534.
[23] M. Steiger, Crystal growth in porous materials - I: The crystallization pressure of large crystals, J. Cryst. Growth 282 (3-4) (2005) 455–469.
[24] M. Steiger, Crystal growth in porous materials - II: Influence of crystal size on the crystallization pressure, J. Cryst. Growth 282 (3-4) (2005) 470–481.
[25] R.J. Flatt, Salt damage in porous materials: how high supersaturations are generated, J. Cryst. Growth 242 (3-4) (2002) 435–454.
[26] O. Coussy, Deformation and stress from in-pore drying-induced crystallization of salt, J. Mech. Phys. Solids 54 (8) (2006) 1517–1547.
[27] R.M. Espinosa-Marzal, G.W. Scherer, Advances in Understanding Damage by Salt Crystallization, Acc. Chem. Res 43 (6) (2010) 897–905.
[28] L.A. Rijniers, P. Magusin, H. Huinink, L. Pel, K. Kopinga, Sodium NMR relaxation in porous materials, J. Magn. Reson. 167 (2004) 25–30.
[29] R.J. Flatt, F. Caruso, A.M.A. Sanchez, G.W. Scherer, Chemo-mechanics of salt damage in stone, Nat. Commun. 5 (1) (2014), 4823.
[30] S. Scrivano, L. Gaggero, An experimental investigation into the salt-weathering susceptibility of building limestones, Rock Mech. Rock Eng. 53 (12) (2020) 5329–5343.
[31] A.E. Charola, S.Z. Lewin, Efflorescences on building stones - SEM in the characterization and elucidation of the mechanisms of formation, 1979.
[32] A.M. Neville, Properties of Concrete, Wiley, 1963.
[33] V. Fassina, Salt efflorescence on the marble slabs of S. Maria dei Miracoli church: a survey on their origin and on the methodology of their removal, s.n, Berlin, Germany, 1996.
[34] F. Madruga, J. Saavedra, M.T. Martín Patino, Eflorescencias y costras sobre areniscas de Villamayor. Ensayos de laboratorio, Mater. De. Constr. 44 (234) (1994) 39–44.
[35] T.D. Goncalves, Salt decay and salt mixtures in the architectural heritage: a review of the work of Arnold and Zehnder, Int J. Arch. Herit. (2022).
[36] O. Gomez-Laserna, M.A. Olazabal, H. Morillas, N. Prieto-Taboada, I. Martinez-Arkarazo, G. Arana, J.M. Madariaga, In-situ spectroscopic assessment of the conservation state of building materials from a Palace house affected by infiltration water, J. Raman Spectrosc. 44 (9) (2013) 1277–1284.
[37] A. Fahmy, E. Molina-Piernas, J. Martinez-Lopez, S. Dominguez-Bella, Salt weathering impact on Nero/Ramses II Temple at El-Ashmonein archaeological site (Hermopolis Magna), Egypt, Herit. Sci. 10 (1) (2022).
[38] G.A. Novak, A.A. Colville, Efflorescent mineral assemblages associated with cracked and degraded residential concrete foundations in Southern-California, Cem. Concr. Res 19 (1) (1989) 1–6.

[39] C. Garcia-Florentino, M. Maguregui, H. Morillas, U. Balziskueta, A. Azcarate, G. Arana, J.M. Madariaga, Portable and Raman imaging usefulness to detect decaying on mortars from Punta Begona Galleries (Getxo, North of Spain), J. Raman Spectrosc. 47 (12) (2016) 1458–1466.

[40] H. Morillas, I. Marcaida, M. Maguregui, J.A. Carrero, J.M. Madariaga, The influence of rainwater composition on the conservation state of cementitious building materials, Sci. Total Environ. 542 (2016) 716–727.

[41] Q.W. Qiu, A state-of-the-art review on the carbonation process in cementitious materials: Fundamentals and characterization techniques, Constr. Build. Mater. 247 (2020).

[42] C. Dow, F.P. Glasser, Calcium carbonate efflorescence on Portland cement and building materials, Cem. Concr. Res 33 (1) (2003) 147–154.

[43] I. Fernandes, M.A.T.M. Broekmans, Alkali-silica reactions: an overview. Part I, Metallogr. Microstruct. 2 (4) (2013) 257–267.

[44] F. Puertas, M. Palacios, T. Vazquez, Carbonation process of alkali-activated slag mortars, J. Mater. Sci. 41 (10) (2006) 3071–3082.

[45] Z.H. Zhang, J.L. Provis, A. Reid, H. Wang, Fly ash-based geopolymers: the relationship between composition, pore structure and efflorescence, Cem. Concr. Res 64 (2014) 30–41.

[46] M.A. Longhi, E.D. Rodriguez, B. Walkley, Z.H. Zhang, A.P. Kirchheim, Metakaolin-based geopolymers: Relation between formulation, physicochemical properties and efflorescence formation, Compos Part B-Eng. (182) (2020).

[47] D. Benavente, P. Brimblecombe, C.M. Grossi, Thermodynamic calculations for the salt crystallisation damage in porous built heritage using PHREEQC, Environ. Earth Sci. 74 (3) (2015) 2297–2313.

[48] C. Rodriguez-Navarro, E. Doehne, E. Sebastian, Influencing crystallization damage in porous materials through the use of surfactants: experimental results using sodium dodecyl sulfate and cetyldimethylbenzylammonium chloride, Langmuir 16 (3) (2000) 947–954.

[49] C. Rodriguez-Navarro, L.L. Fernandez, E. Doehne, E. Sebastian, Effects of ferrocyanide ions on NaCl crystallization in porous stone, J. Cryst. Growth 243 (3-4) (2002) 503–516.

[50] C. Selwitz, E. Doehne, The evaluation of crystallization modifiers for controlling salt damage to limestone, J. Cult. Herit. 3 (3) (2002) 205–216.

[51] E. Ruiz-Agudo, C. Rodriguez-Navarro, E. Sebastian-Pardo, Sodium sulfate crystallization in the presence of phosphonates: Implications in ornamental stone conservation, Cryst. Growth Des. 6 (7) (2006) 1575–1583.

[52] V. Tantayakom, H.S. Fogler, P. Charoensirithavorn, S. Chavadej, Kinetic study of scale inhibitor precipitation in squeeze treatment, Cryst. Growth Des. 5 (1) (2005) 329–335.

[53] E. Molina, G. Cultrone, E. Sebastián, F.J. Alonso, L. Carrizo, J. Gisbert, O. Buj, The pore system of sedimentary rocks as a key factor in the durability of building materials, Eng. Geol. 118 (3-4) (2011) 110–121.

[54] C.M. Rodríguez Navarro, Causas y mecanismos de alteración de los materiales calcáreos de la catedrales de Granada y Jaén, Universidad de Granada, 1994.

[55] D. Benavente, M.A. García del Cura, R. Fort, S. Ordóñez, Durability estimation of porous building stones from pore structure and strength, Eng. Geol. 74 (1) (2004) 113–127.

[56] R.J. Schaffer, The Weathering of Natural Building Stones, Taylor & Francis, 2016.

[57] S.J.C. Granneman, E. Ruiz-Agudo, B. Lubelli, Rv Hees, C. Rodriguez-Navarro, Study on effective modifiers for damaging salts in mortar, 2014.

[58] D. Gulotta, S. Godts, T. De Kock, M. Steiger, Comparative estimation of the pore filling of single salts in natural stone, in: A.K.B. Lubelli, W. Quist (Eds.), SWBSS 2021: fifth International Conference on Salt Weathering of Buildings and Stone Sculptures, TU Delft Open, Delft, 2021, pp. 79–88.

[59] C. Monnin, J. Schott, Determination of the solubility products of sodium-carbonate minerals and an application to trona deposition in Lake Magadi (Kenya), Geochim Cosmochim. Ac 48 (3) (1984) 571–581.

[60] D. Parkhurst, C.A.J. Apello, Description of Input and Examples for PHREEQC Version 3?a Computer Program for Speciation, Batch-Reaction, One-Dimensional Transport, and Inverse Geochemical Calculations, CreateSpace Independent Publishing Platform 2014.

[61] W. Stumm, J.J. Morgan, Aquatic Chemistry: Chemical Equilibria and Rates in Natural Waters, Wiley, 2012.

[62] A. Shchukarev, J. Rosenqvist, S. Sjoberg, XPS study of the silica-water interface, J. Electron Spectrosc. 137 (2004) 171–176.

[63] B. Nowack, Environmental chemistry of phosphonates, Water Res. 37 (11) (2003) 2533–2546.

[64] B. Nowack, A.T. Stone, Adsorption of phosphonates onto the goethite-water interface, J. Colloid Interface Sci. 214 (1) (1999) 20–30.

[65] L. Addadi, S. Weiner, Control and Design Principles in Biological Mineralization, Angew. Chem. Int Ed. 31 (2) (1992) 153–169.

[66] E. Ruiz-Agudo, Prevención del daño debido a la cristalización de sales en el patrimonio histórico construido mediante el uso de inhibidores de la cristalización, Universidad de Granada, Granada, 2007.

[67] M.N. Rad, N. Shokri, Nonlinear effects of salt concentrations on evaporation from porous media, Geophys. Res. Lett. 39 (2012).

[68] M. Steiger, S. Asmussen, Crystallization of sodium sulfate phases in porous materials: The phase diagram Na2SO4-H2O and the generation of stress, Geochim. Cosmochim. Acta 72 (17) (2008) 4291–4306.

[69] R.M. Espinosa Marzal, G.W. Scherer, Crystallization of sodium sulfate salts in limestone, Environ. Geol. 56 (3) (2008) 605–621.

[70] M. Urosevic, E. Sebastián Pardo, E. Ruiz-Agudo, C. Cardell, Physical and mechanical appraisal of two carbonatic stones widely used in the architectural heritage of eastern Andalusia, Spain, Mater. De. Constr. 61 (301) (2011) 93–114.

[71] D.G. Leaist, R.A. Noulty, Multicomponent diffusion of aqueous sodium carbonate and aqueous sodium bicarbonate, Can. J. Chem. 63 (8) (1985) 2319–2323.

[72] T.A. Saidov, L. Pel, K. Kopinga, Crystallization pressure of sodium sulfate heptahydrate, Cryst. Growth Des. 15 (5) (2015) 2087–2093.